1   **Optically pumped magnetometers disclose magnetic field components of the muscular**

2   **action potential**

3   Philip J. Broser[a]*, Thomas Middelmann[b], Davide Sometti[c], Christoph Braun[c,d,e]

4   [a] *Children's hospital of eastern Switzerland, Sankt Gallen, Switzerland*

5   [b] *Physikalisch technische Bundesanstalt, Berlin, Germany*

6   [c] *MEG Center, University of Tübingen, Germany*

7   [d] *Hertie-Institute for Clinical Brain Research, Tübingen, Germany*

8   [e] *CIMeC, Center for Mind/Brain Sciences, Tübingen, Germany*

9

10   *Corresponding author

11   Dr. Philip J. Broser (ORCID iD: 0000-0003-4477-1432)

12   Philip.Broser@kispisg.ch

13   Philip.Broser@icloud.com

14   Ostschweizer Kinderspital,

15   Neuropediatric Department

16   Claudiusstrasse. 6

17   CH – 9006 St. Gallen

18   Tel. +41 71 243 19 28

19

24 **ABSTRACT**

25 **Aim:** To track the magnetic field generated by the propagating muscle action potential (MAP).

26 **Method:** In this prospective, proof of principle study, the magnetic activity of the intrinsic foot

27 muscle after electric stimulation of the tibial nerve was measured using optically pumped

28 magnetometers (OPMs). A classical biophysical electric dipole model of the propagating MAP

29 was implemented to model the source of the data.

30 **Results:** The signal profile generated by the activity of the intrinsic foot muscles was measured

31 by four OPM devices. Three devices were located above the same muscle to compare the

32 direction and the strength of the magnetic signal while propagating along the muscle.

33 **Interpretation:** OPM devices allow for a new, non-invasive way to study MAP patterns. Since

34 magnetic fields are less altered by the tissue surrounding the dipole source compared to electric

35 activity, a precise analysis of the spatial characteristics and temporal dynamics of the MAP is

36 possible. The classic electric dipole model explains major but not all aspects of the magnetic

37 field. The field has longitudinal components generated by intrinsic structures of the muscle

38 fibre. By understanding these magnetic components, new methods could be developed to

39 analyse the muscular signal transduction pathway in greater detail.

40

41 **What this paper adds:**

42 - Technological concepts to record and analyse the small magnetic fields generated by

43 electric muscular activity

44 - Model to link the signals measured by the OPM sensors to the underlying physiology

45 - Insights into the propagation of muscle action potential and the sequential control of

46 motor activity

47 **Abbreviations:**

48 - OPM: optically pumped magnetometer

49 - MAP: muscle action potential

1   Introduction

The molecular control of the contractile apparatus of the skeletal muscle is critically dependent on the muscle action potential (MAP) propagating along the muscle fibre after initiation at the neuromuscular endplate (Moritani T, Stegeman D, Merletti R, 2004). After activation of the postsynaptic membrane by acetylcholine (AcH), several different positively charged ions can cross these channels (Martonosi, 2000). The influx of these ions depolarises the membrane of the muscle fibre, the voltage gated sodium channels open and a MAP is generated which propagates along the muscle fibre in both the proximal and distal directions (Farina and Merletti, 2004). In contrast to the neural action potential, the MAP is established by sodium, potassium and calcium ions (Martonosi, 2000). The speed of the MAP is an estimated 4–6 m/s (Farina and Merletti, 2004) slower than the action potentials of motor neurons (around 50 m/s, Ghezzi et al., 1991). Similar to the neuronal action potential (Wikswo et al., 1980), the MAP leads to a specific magnetic field (Zuo et al., 2020), which can be measured by superconducting quantum interference devices (SQUIDs, Reincke, 1993) or optically pumped magnetometers (OPMs) (Broser et al., 2018). However, there are significant anatomical differences between the axon of a neuron and a muscle fibre. First of all, the cross-sectional diameter of a muscle fibre is in the range of 20–100 μm, whereas an axon is typically 1 μm in diameter. Further, the membrane of a muscle fibre has a high number of cylindrical infoldings, known as T-tubuli. The MAP is propagated deep in the myocyte along the T-tubuli, in close proximity to the contractile apparatus. The MAP along the T-tubuli generates a radial current that creates an additional magnetic field component in the longitudinal direction of the fibre.

The magnetic fields generated by the MAP are in the range of 0.01 to 0.1 nanotesla (nT), and therefore, special devices are required to record these small magnetic fields. OPMs are newly developed sensors (Mhaskar et al., 2012; Colombo et al., 2016; Labyt et al., 2019)

75   that can measure these small magnetic fields. Unlike SQUIDs (Reincke, 1993), OPMs are much

76   smaller and can be placed in close proximity to the muscle.

77   In this study, we developed a measurement setup to record the MAP of the intrinsic foot

78   muscles generated after electric stimulation of the tibial nerve using OPM devices. The

79   magnetic field was measured in two orthogonal directions. The signal-to-noise ratio and

80   reproducibility was tested. Given that magnetic field distributions are geometrically complex,

81   and an intuitive guess of the source of the magnetic field might be misleading, we implemented

82   a classical electric dipole model to explain the sources of the magnetic fields.

83   The model is based on an electric dipole propagating along the muscle fibre. The muscle

84   fibre was approximated as a finite wire, and the MAP was modelled according to the study by

85   Rosenfalck (1969).

86   Given that this model explains some but not all aspects of the magnetic field, a second

87   model based on a moving magnetic dipole was in addition tested. This model is motivated by

88   the estimation of the radial currents inside the muscle as found by Henneberg and Roberge

89   (1997). In comparison to the first model, this model takes into consideration the radial currents

90   resulting from the MAP propagating along the T-tubuli and thus generating a magnetic field

91   component into the longitudinal direction of the muscle fibre.

92   **2   METHOD**

93   *2.1   Recording of the magnetic activity of the MAP*

94   A single-subject, proof of principal study was conducted at the MEG Center of the

95   University of Tübingen in January 2020. The experiment was designed specifically to record

96   the magnetic activity of the intrinsic foot muscles after tibial nerve stimulation.

97   The electric stimulus used to stimulate the nerve interferes with the OPM sensors for

98   about 10 ms. Thus, the stimulation site was chosen such that the time delay between stimulation

99   and muscle activity was greater than 10 ms. Therefore, the tibial nerve was stimulated at the

100   level of the knee.

101   The study aimed to record the activity of the abductor hallucis brevis. This muscle is

102   innervated by the tibial nerve (Figure 1A). The abductor hallucis brevis muscle is located at the

103   medial border of the foot (Figure 1C) and was localised by palpation by an experienced clinical

104   doctor (PB). The muscle inserts on the OS calcaneus. The muscle body is thick and flattens as

105   it stretches forward to the big toe. The muscle ends in a common tendon with the flexor hallucis

106   brevis. This tendon ends on the medial surface of the base of the first proximal phalanx (big

107   toe, hallux). Additional intrinsic foot muscles are located close to the big toe (musculus flexor

108   hallucis and musculus adductor hallucis). These muscles are also innervated by the tibial nerve,

109   and therefore, their MAP could add signal components to the recording (Figure 1C).

110   During the experiment, the tibial nerve was stimulated by two electrodes placed on the

111   skin on the dorsal side of the knee (Figure 1B) at a distance of about 40 cm proximal to the

112   ankle. A series of four OPMs (labelled S, T, U and V) were positioned longitudinal to the medial

113   border of the foot (Figure 1B). The OPM devices were placed such that the z-axis of the sensor

114   pointed towards the plantar side of the foot, and the y axis pointed in the lateral direction (Figure

115   1B). The distance between neighbouring sensors was 3.5 cm. The sensors T, U and V were

116   located above the musculus abductor hallucis and were therefore the main sensors of interest in

117   the study. The participant (a co-author of this paper) gave his informed consent to participate

118   in the study and agreed to the publication of his data. The study was performed in accordance

119   with the Declaration of Helsinki (World Medical Association, 2001).

120   *2.2   Experimental setup*

121   The detailed experimental procedure (Figure 1A,B) began with the subject (a 30-year-

122   old male) lying on a comfortable bed inside of a magnetic shielded room (Ak3b, VAC

123   Vacuumschmelze, Darmstadt, Germany). The subject rested his right leg on a pillow. The right

124   foot was placed in a cardboard box (25 × 15 cm) filled with rigid foam with a cavity to

125   accommodate the foot. The bottom of the box had four slots to host the OPMs (QZFM-gen-1.5,

126   QuSpin Inc., Louisville, CO, USA). These magnetometers were based on an optically detected

127   zero-field resonance in hot rubidium vapor, which was contained in a vapor cell measuring 3 ×

128   3×3 mm^3. The centre of the cell had a distance of 6.2 mm to the exterior of the housing, which

129   measured $13 \times 19 \times 85$ mm^3. This small size allows for easy handling of these sensors and

130   flexibility to adapt the sensors to the specific geometrical situation (Alem et al., 2015; Boto et

131   al., 2017, Osborne et al., 2018). The OPMs are capable of measuring two components of the

132   magnetic field vector: the y and z direction (Figure 1B). They provided a magnetic field

133   sensitivity in the order of $15 \ \mathrm{fT}/\sqrt{\mathrm{Hz}}$ in a bandwidth of 3–135 Hz and a dynamic range of a few

134   nT. To adapt to a non-zero magnetic background field, the sensors were equipped with internal

135   compensation coils, which can cancel magnetic background fields with a strength of up to

136   200 nT in the sensing vapor cell.

137   Our OPM measurement system consisted of a total of five OPMs, which simultaneously

138   recorded the magnetic field in two orthogonal directions (y and z). As described above, four

139   sensors were placed inside the slots of the box along a line running across the medial plantar

140   side of the foot (Figure 1C). A fifth sensor was placed just outside the box to measure the

141   magnetic background activity.

142   In order to synchronise the muscular activity with the recording system, the MAP was

143   recorded after electric stimulation of the nerve. To this end, self-adherent electrodes were

144   placed on the skin of the subject in close proximity to the tibial nerve (Figure 1A,B) at the level

145   of the knee. The stimulator (System Plus Fire, Micromed, Venice, Italy) was placed outside the

146   magnetically shielded room, and the two-electrode cables (cathode and anode) were routed

147   through small holes into the magnetic chamber. The tibial nerve was stimulated with a

148   monopolar square wave pulse of 500 µs duration and an intensity of 35 mA (Broser and

149   Luetschg, 2020).

150   While providing electrical stimuli, a simultaneous trigger signal was sent to the data

151 acquisition system of our MEG system (CTF Omega 275, Coquitlam, BC, Canada). This signal

152 was used to synchronise both the stimulation and the recording. For the recording of the

153 neuromagnetic signal, a sampling rate of 2343.8 samples/s was used. The OPM system

154 delivered two analogue signals for the magnetic field strength in the y and z direction for each

155 sensor. A low-pass filter of 100 Hz was applied to the analogue signal. The OPM system and

156 the analogue digital converter of the recording system both had an intrinsic delay. This delay

157 was measured to be 6.2 ms. The timing of the data was post hoc adjusted so that the stimulus

158 was applied at t = 0 s. During the experiment, 10 electric stimuli were applied, and the evoked

159 magnetic muscular activity was recorded. The plots and analyses of the OPM data was

160 performed in R (R Core Team, Vienna, Austria).

161 *2.3 Model of the magnetic field of the MAP*

162 *2.3.1 Geometrical considerations*

163   The measurement setup was arranged such that the musculus abductor hallucis was in

164 the xy plane below the OPM sensors T, U and V. Therefore, the position of the MAP on the

165 fibre could be parameterised by:

$$\vec{L}(s) = \begin{pmatrix} x_0 + s*cos(\alpha) \\ y_0 + s*sin(\alpha) \\ d \end{pmatrix}, \text{ with } \frac{d\vec{L}}{ds} = \begin{pmatrix} cos(\alpha) \\ sin(\alpha) \\ 0 \end{pmatrix} \tag{1}$$

167 where $\vec{L}(s)$ is the position pointing to the present position of the MAP; s is the index to

168 parameterise the longitudinal direction of the muscular fibre; x_0 and y_0 are the translation of

169 the fibre in relation to the OPM sensor in the x and y plane, respectively; d is the minimal

170 distance between the OPM sensor and muscle fibre; and α is the angle of the muscle fibre in

171 the xy plane defined by the measurement setup.

172   Without loss of generality the simulation of each sensor was conducted with the

173 assumption that the sensor is located at position (0,0,0). Therefore, for each OPM sensor and

174   each L, the point $\vec{L}(0)$ corresponded to the point of plumb. Figure 2B shows this geometrical

175   arrangement graphically.

176   *2.3.2   MAP*

177   According to the work by Farina and Merletti (2001), the voltage at the site of the two

178   propagating MAPs can be described by:

179     $$\Delta V_{longitudinal}(s,t) = \psi_1\big(s - s_{endplate} - v_{AP} * t\big) + \psi_2(s - s_{endplate} + v_{AP} * t) \quad (2)$$

180   where ψ_1 and ψ_2 being the two MAPs propagating in the proximal and distal directions,

181   respectively. Rosenfalck (1969) described the transmembrane voltage of the MAP using:

182     $$V(s)_{membrane} = \begin{pmatrix} A*s^3 e^{-s} + B; s>0 \\ 0; s \leq 0 \end{pmatrix} \quad (3)$$

183   where $A = 96 \frac{mV}{mm^3}$ and B = -90 mV (Figure 2C). The longitudinal voltage difference can be

184   obtained by differentiation:

185     $$\psi_{1,2}(t) = \left(\frac{dV_{membrane}}{ds}\right)(t). \quad (4)$$

186   The longitudinal voltage gradient $\Delta V_{longituidnal}(s,t)$ was divided by the longitudinal

187   resistance $r_{ix} = 173\,\Omega * cm = 17.3\,\Omega * mm$ (Henneberg and Roberge, 1997) to obtain an

188   estimate of the longitudinal current. The estimation of the current and current density of the

189   radial current in the T-tubuli was more difficult to obtain. Henneberg and Roberge (1997)

190   created a rigorous mathematical approach and values for discovering the radial current. The

191   sum of the currents in the T-tubuli of a given muscular segment is similar in magnitude to the

192   longitudinal current (Henneberg and Roberge, 1997).

193   *2.3.3   Magnetic field of propagating action potentials in general*

194   For isolated nerves, the electric field of a propagating action potential generates a

195   magnetic field (Wikswo et al., 1980; Reincke, 1993) with an absolute magnetic field strength

196   of about 70 pT at a distance of about 1 cm from the nerve surface. Wikswo et al. (1980) showed

197   that when the action potential passes the sensor, a characteristic biphasic magnetic signal can

198   be recorded. The turning point of the signal graph correlates with the action potential below the

8

199   sensor. In a previous study, we recorded the magnetic field of the muscular activity of the

200   intrinsic hand muscles (Broser et al., 2018). Equation (2) lays the groundwork for the finite

201   wire model to describe the magnetic field generated by the propagating MAP.

202   *2.4   Finite wire model*

203   This model assumes that each propagating action potential can be approximated as a

204   finite wire (Figure 2D-1). Without loss of generality, from here on, only one of the two action

205   potentials is considered at a time. The magnetic field of this finite wire can be calculated using

206   the Biot–Savart law (Westgard J., 1997):

207

$$\vec{B}(s) = \frac{\mu_0}{4\pi} \int_s^{s-\Delta s} I(s-t) * \frac{\vec{R}(t) \times \overline{\frac{dL}{ds}}}{|R|^3} \, dt \;\; \text{with}$$

208

$$I(t) = \frac{A_{fibre} *}{r_{ix}} * \left(\frac{dV_{membrane}}{ds}\right)(t), \; R(s) = \begin{pmatrix} 0 \\ 0 \\ 0 \end{pmatrix}_{Position_{OPM}} - L(s) = \begin{pmatrix} -x_0 - s*cos(\alpha) \\ -y_0 - s*sin(\alpha) \\ -d \end{pmatrix} \quad (5)$$

209   where s is the index to parameterise the position of the MAP, $\Delta s = 15$ mm and is the longitudinal

210   extent of the MAP (compare with Equation 3 and Figure 2C), A_{fibre} is the area of electric active

211   tissue in mm^2, $r_{ix} = 17.3 \, \Omega * mm$ and I is the longitudinal current as calculated from Equation

212   (3). The sign of I is positive if the movement of positive charges is in the direction of the index

213   parameter t.

214   Remark: A_{fibre} is dependent on the activated numbers of neuromuscular units are and the total

215   thickness of electric activate muscle tissue.

216   The experimentally determined parameters were A_{fibre}, α, y_0, x_0 and d. The parameter d

217   was estimated by muscle ultrasound to be 8 mm. The computations for the finite wire model

218   were performed using Maple™ (Waterloo, ON, Canada). One simulated example of a resulting

219   magnetic field generated by an action potential propagated according to Figure 2D-1 is shown

220   in Figure 2D-2 in the B field in the y direction and Figure 2D-3 in the B field in the z direction.

221   To quantify the residual relative error of the fit, the L^2 norm on the interval -40 to 40 mm off

9

222 the residual function $\vec{R}(s) := \vec{B}(s) - \overrightarrow{OPM}(s)$ was calculated and normalized by the total

223 signal: $\overrightarrow{relErr} := \frac{[R]_{L2}}{[OPM]_{L2}}$.

2.5 Magnetic dipole model

225   Based on our empiric findings, we developed a second model. This model assumes that

226 the dense T-tubuli network in the muscular fibre generates a net radial current. This current

227 then generates a magnetic dipole. Given the finite expansion of the MAP, we hypothesised that

228 this finite magnetic component can be approximated by a magnetic dipole. The magnetic field

229 generated at the site of the OPM sensor would than calculate to:

$$\vec{B}(t) = \frac{\mu_0}{4\pi} \frac{\vec{R}(t)*3*\left(\vec{m}\cdot\vec{R}(t)\right) - \vec{m}*\left|\vec{R}(t)\right|^2}{\left|\vec{R}(t)\right|^3} \tag{6}$$

231 with the dipole vector $\vec{m}$ pointing into the direction of the fibre:

$$\vec{m} = \begin{pmatrix} cos(\alpha)*m \\ sin(\alpha)*m \\ 0 \end{pmatrix} \tag{7}$$

233 where $m[A \cdot m^2]$ is the magnitude of the dipole moment. The experimentally determined

234 parameters were m, α, y_0, x_0 and d. Similar to the finite wire model we simulated the propagation

235 of the muscular action potential along the muscular fibre.

3 Results

3.1 OPM signal

238   The tibial nerve was stimulated at the level of the knee with 35-mA reliably elicited

239 muscular contractions in the intrinsic foot muscles. As shown in Figure 3, the first signal after

240 stimulation could be detected from the OPM sensors T, U and V about 12 ms after stimulation.

241 In order to estimate the conduction velocity along the tibial nerve, the length of the nerve and

242 the time delay between stimulus onset and the arrival of the signal at the muscle was considered.

243 The lower leg of the subject had a length of 40 cm (knee to medial malleolus), and the distance

244 between the musculus abductor hallucis and the medial malleolus was estimated to be 8 cm.

10

245   Synaptic transmission typically takes 1 ms. This results in a grossly estimated nerve conduction

246   speed of NCS = (40 cm + 8 cm)/(12 ms - 1 ms) = 0.48 m/11 ms = 43 m/s.

247   A total of 10 stimuli were applied to the nerve. The recorded time-dependent magnetic

248   fields for the sensors in the z and y directions are shown in Figure 3. The signal profiles of the

249   individual traces are quite stable and show only moderate variability. The means and standard

250   deviations of the peak-to-peak amplitude of the signals were 0.0094 ± 0.0021 nT for sensor S,

251   0.0648 ± 0.0145 nT for sensor T, 0.0759 ± 0.0051 nT for sensor U and 0.0496 ± 0.0029 nT for

252   sensor V. The background signals were 0.0026 ± 0.0007 nT for sensor S, 0.0026 ± 0.0004 nT

253   for sensor T, 0.0038 ± 0.0007 nT for sensor U and 0.0024 ± 0.0006 nT for sensor V. The signal-

254   to-noise ratios were therefore 4:1 for sensor S, 24:1 for sensor T, 20:1 for sensor U and 19:1

255   for sensor V. Based on the high signal-to-noise ratio, further analysis of the measured data of a

256   single stimulation was conducted. Wikswo et al. (1980) demonstrated that for the propagating

257   axonal action potential, the magnetic flux shows a change in phase while the action potential

258   passes the sensor. The recorded OPM signals showed a similar bi/triphasic profile (Figure 4)

259   with a zero crossing at 18 ms for sensor S, 20 ms for sensor T, 17 ms for sensor U and 17 ms

260   for sensor V. However, given the larger spatial extent of the MAP, the shape of the magnetic

261   flux signal is more complex.

262   *3.2   Finite wire model*

263   In order to account for the complexity of the MAP signal, a manual parameter search

264   was conducted in order to fit the finite wire model onto the data. Sensors T, U and V were

265   anatomically well-located above the musculus abductor hallucis. The muscles beneath sensor

266   S were less well-defined. Therefore, the analysis focused on the sensors T, U and V. By

267   approximating the velocity of the MAP with $v_{AP} = 5\frac{m}{s}$ (Farina and Merletti, 2004), we could

268   project the time-depended measured magnetic field strength from the time space into the

269   location space using the formula $z(t) = (t - t_{offset}) \cdot v_{AP}$. The measurement data were

11

270   transferred into the location space (Figure 4), and a manual parameter search was conducted

271   with the aim to approximate the strength and signal characteristics.

272   For each dataset, the model parameters A_{fibre}, α, y_0 and x_0 were systematically altered,

273   and the signal profiles were visually compared. First the angle α was set to $\alpha = 0°$ or $\alpha = 180°$

274   in order to match the polarity of the first peak in By and Bz direction. Second the parameter

275   A_{fibre} was screened to obtain a similar amplitude of the signal in the y direction for all three

276   sensors in consideration (T,U,V). Third the t_{offset} was fine tuned to match the local maxima

277   and minim. Finally, the parameter y_0 was varied to match the magnitude of the Bz component.

278   No further parameters had to be adjusted (see Table 1). In order to quantify the goodness of fit

279   the L2 norm of the residual function normalized by the L2 norm of the signal function was

280   calculated (see Table 2).

281   Interestingly, for sensors T, U and V, only the direction of the propagating action

282   potential (downwards $\alpha = 0°$ or upwards $\alpha = 180°$) and the time offset (t_{offset}) had to be

283   defined. All other parameters were similar for all three sensors. The electric active fibre area

284   A_{fibre} was the same for all three sensors.

285   Based on these parameters, the finite wire model predicted that the MAP propagates beneath

286   sensor T towards the big toe. In addition, it predicted at least one further action potential that

287   propagates in the opposite direction towards the heel and passes sensors U and V. Given that

288   the angles between the two predicted MAPs changed from upwards ($\alpha_T = 180°$) to downwards

289   ($\alpha_{U,V} = 180°$), the MAPs were probably initiated between sensors T and U. This finding

290   directly suggests that the neuromuscular endplate is located between these two sensors.

291   Comparing the signal traces of the recorded (Figure 4, red traces) and the modelled

292   signals (Figure 4, black traces) reveals a relevant difference that cannot be explained by the

293   finite wire model. In the Y direction, the sensors U and V show a triphasic signal trace. The

294   finite wire model only generates a triphasic signal trace if one considers an obscure geometrical

295   arrangement. Triphasic magnetic signal traces are typical for moving magnetic dipoles.

296   We therefore empirically tested if a magnetic dipole model (see Supplementary Figure

297   1) could explain this feature. A parameter search as described above was conducted

298   (Supplementary Table 1) and the signal traces were visualized (see Supplementary Figure 2).

299   As expected, a simulation based on a magnetic dipole returned a triphasic signal trace in the Y

300   direction but a significant angulation of the propagating direction (Supplementary Table 1) was

301   necessary. The residual error for both directions was smaller for the magnetic dipole model

302   when compared to the finite wire model (see Supplementary Table 2).

303   **4   Discussion**

304   In this study, we used OPMs to record the magnetic field generated by the propagating

305   action potential of the intrinsic foot muscles. The MAP was triggered by electric stimulation of

306   the supplying nerve in order to elicit synchronised and timely defined MAP of a high number

307   of simultaneously activated neuromuscular units. The study specifically focused on the

308   musculus abductor hallucis brevis. The three sensors located above this muscle picked up the

309   magnetic component of the MAP with a signal that was greater than 10 times the background

310   activity.

311   As has been previously studied for the nerve AP, we could record a flipping of the B

312   field in the By and Bz direction as the MAP passed the sensor. A manual parameter search was

313   conducted to fit a finite wire model to the data. The only one parameter (A_{fiber}) to be fitted to

314   the data was kept the same for all three sensors in consideration. In addition, based on

315   geometrical anatomical considerations the angle of the propagating direction was selected to be

316   either up or downwards. No further adjustments were necessary. The finite wire model could

317   reasonably reproduce the signal traces and the residual error was measure by the L_2 metric. The

13

318   error was small for the Bz direction but large for the By direction. Based on this model we were

319   able to predict the location of the neuromuscular endplate.

320   Although the model explained major features of the recorded data, the triphasic profile

321   of the measured magnetic fields in the By direction could not be explained by the finite wire

322   model. We therefore empirically tested a magnetic dipole model. This model shows the

323   expected signal profiles and the residual errors are smaller in By and Bz direction, but a

324   significant angulation of the dipole would be required which is not supported by the anatomical

325   situation. Therefore, we hypothesize that a combination of the two approaches would model

326   the magnetic field best. However, to do so the recording of the magnetic field in all three spatial

327   directions is required.

328

4.1   Limitations

330   Even though the study revealed some very interesting findings, it had some relevant

331   limitation. First the OPM sensor used, only recorded the magnetic field in the Z and Y direction.

332   The field strength in X direction could not be measured and a different model might be obtained

333   when the field in this direction would have been recorded.

334   Second, the study focused on an intrinsic foot muscle. This approach was chosen in

335   order to have a sufficient time delay between electric stimulation and recording. But there are

336   several other muscles in close proximity and so the evaluation of the muscular action potential

337   for the whole extend of the muscle is difficult. In a future study ideally a large muscle with a

338   linear anatomical orientation should be used like the rectus femoris. This muscle would allow

339   to observe the propagation of the muscular action potential over al longer distance. Third, as

340   yet the bandwith of the OPM sensors is limited and a precise temporal and spatial localization

341   of the signal is restricted. Fourth, the study was based on a stimulated approach. That means

342   the supplying nerve was electrically stimulated in order to record the magnetic field. But for a

343   detailed analysis of the neuro- muscular physiology an approach based on the resting activity,

344   the reflex response or the voluntary activity is necessary. This is especially important to

345   establish this method in clinically medicine.

346   *4.2   Outlook*

347   We are in the process of planning a new set of experiments using the latest generation

348   of OPM devices to record the magnetic field in all three spatial directions. Given the high

349   signal-to-noise ratio shown by the magnetic component of the MAP, we plan to conduct the

350   next series of experiments based on a voluntary muscular activation paradigm or based on the

351   response of the monosynaptic reflex.

352 **References**

353 Alem O, Sander TH, Mhaskar R, LeBlanc J, Eswaran H, Steinhoff U, Okada Y, Kitching J,

354   Trahms L, Knappe S. Fetal magnetocardiography measurements with an array of

355   microfabricated optically pumped magnetometers. Phys. Med. Biol. 2015;60:4797.

356 Boto E, Meyer SS, Shah V, et al. A new generation of magnetoencephalography: room

357   temperature measurements using optically-pumped magnetometers. Neuroimage

358   2017;149:404-14. https://doi.org/10.1016/j.neuroimage.2017.01.034

359 Broser PJ, Knappe S, Kajal DS, et al. Optically pumped magnetometers for magneto-

360   myography to study the innervation of the hand. IEEE Trans. Neural. Syst. Rehabil.

361   Eng. 2018;26(11):2226-30. https://doi.org/10.1109/TNSRE.2018.2871947

362 Broser PJ, Luetschg J. Elektroneurograsche und elektromyographische Diagnostik in der

363   Neuropaediatrie [Electromyography and Electro-neurography in the Neuropediatric

364   Diagniostic   Process].   Klinische   Neurophysiologie   2020;51:73-81.

365   https://doi.org/10.1055/a-0993-6459

366 Colombo AP, Carter TR, Borna A, Jau Y-Y, Johnson CN, Dagel AL, Schwindt PDD. Four-

367   channel optically pumped atomic magnetometer for magnetoencephalography. Opt.

368   Express 2016;24:15403-16.

369   https://doi.org/10.1364/OE.24.015403

370 Farina D, Merletti R. A novel approach for precise simulation of the EMG signal detected by

371   surface   electrodes.   IEEE   Trans.   Biomed.   Eng.   2001;48(6):637-46.

372   https://doi.org/10.1109/10.923782

373 Farina D, Merletti R. Estimation of average muscle fiber conduction velocity from two-

374   dimensional surface EMG recordings. J. Neurosci. Methods 2004;134(2):199-208.

375   https://doi.org/10.1016/j.jneumeth.2003.12.002

376 Ghezzi A, Callea L, Zaffaroni M, Zibetti A, Montanini R. Study of central and peripheral motor

377   conduction in normal subjects. Acta Neurol. Scandmavica 1991;84(6), 503-6.

378   Henneberg KA, Roberge FA. Simulation of propagation in a bundle of skeletal muscle fibers:

379   modulation effects of passive fibers. Ann. Biomed. Eng. 1997;25(1):29-45.

380   https://doi.org/10.1007/BF02738536

381   Labyt E, Corsi M, Fourcault W, Laloy AP, Bertrand F, Lenouvel F, Cauffet G, Prado ML,

382   Berger F, Morales S. Magnetoencephalography with optically pumped 4He

383   magnetometers at ambient temperature. IEEE T. Med. Imaging 2019;38:90.

384   Martonosi A. Animal electricity, Ca2+ and muscle contraction: a brief history of muscle

385   research. Acta Biochim. Pol. 2000;47(3):493-516.

386   Mhaskar R, Knappe S, Kitching J. A low-power, high-sensitivity micromachined optical

387   magnetometer. Appl. Phys. Lett. 2012;101:241105.

388   https://doi.org/10.1063/1.4770361

389   Moritani T, Stegeman D, Merletti R. Basic physiology and biophysics of EMG signal

390   generation. In: Merletti R, Parker P, editors. Electromyography: physiology,

391   engineering, and noninvasive applications. Wiley-IEEE Press 2004:1-25.

392   Osborne J, Orton J, Alem O, Shah V. Fully integrated, standalone zero field optically pumped

393   magnetometer for biomagnetism. Proc. SPIE 10548, Steep Dispersion Engineering and

394   Opto-Atomic Precision Metrology XI 2018;105481G:.

395   https://doi.org/10.1117/12.2299197

396   Reincke M. Magnetomyographie mit dem SQUID [Magnetomyography with the SQUID].

397   Biomed. Eng. 1993;38(11):276–81.

398   Rosenfalck P. Intra- and extracellular potential fields of active nerve and muscle fibres: a

399   physico-mathematical analysis of different models. Acta Physiol. Scand. Suppl.

400   1969;321:1-168.

401   Westgard J. Electrodynamic: a concise introduction. New York: Springer, 1997.

402   Wikswo JP, Barach JP, Freeman JA. Magnetic field of a nerve impulse: first

403   measurements. Science 1980;208(4439):53-5. https://doi.org/10.1126/science.7361105

404   World Medical Association. Declaration of Helsinki: ethical principles for medical research

405   involving human subjects. Bull. World Health Organ. 2001;79(4):373-4.

406   Zuo S, Heidari H, Farina D, Nazarpour K. Miniaturized magnetic sensors for implantable

407   magnetomyography.   Adv.   Mater.   Technol.   2020;5:2000185.

408   https://doi.org/10.1002/admt.202000185

409

410 **Tables**

411 Table 1 – Finite wire model predicted parameters

Sensor	α (°)	y_0 (mm)	A_{fibre} (mm^2)	Offset (ms)
S	77	-4	1	-15.71
T	180	10	2	-17.55
U	0	10	2	-16.30
V	0	10	2	-16.30

412 Note: for all OPM sensors, $x_0 = 0$ and $d = 8$ mm.

413

414 Table 2 – Residual Error - Current Modell

415

Sensor	Y – direction	Z – direction
S	2.558	0.750
T	2.341	0.633
U	0.375	0.287
V	2.112	0.432

416

417

19

418 **Supplementary Tables**

419 Supplementary Table 1 – Magnetic dipole model predicted parameters

OPM	U	V	T	S	[Unit]
α	120	120	-160	150	[degree]
$l_{polarity}$	1	-1	1	1	
x_0	-0.005	-0.0005	0.001	0.001	[m]
y_0	0	0	0	0	[m]
m_0	$3.5 \cdot 10^{-10}$	$-3.5 \cdot 10^{-10}$	$-3.5 \cdot 10^{-10}$	$-3.5 \cdot 10^{-10}$	$[A \cdot m^2]$
d	0.008	0.011	0.011	0.0145	[m]
v_{Dipole}	5	5	2.5	5	$[\frac{m}{s}]$

420

421 Supplementary Table 2 – Residual Error - Magnetic Dipole Modell

422

Sensor	Y – direction	Z – direction
S	0.618	1.44
T	0.428	0.464
U	0.417	0.336
V	1.397	0.304

423

20

424 **Figure legends**

425 **Figure 1:** Principal setup of the experiment. (A) Schematic anatomical drawing of the lower

426 leg. The black circle at the level of the knee highlights the area on the skin where the tibial

427 nerve was stimulated. (B) Schematic drawing of the lower leg. Lateral view onto the medial

428 aspect of the lower leg together with the relevant structures and technical equipment. (B1)

429 Location of the self-adherent stimulation electrodes (black = cathode, red = anode). (B2) Tibial

430 nerve. (B3) Intrinsic foot muscles, specifically the musculus abductor hallucis. (B4) Four OPM

431 recording devices. Coordinate system in the upper right. The y axis points out of the drawing

432 area. (C) Position of the four OPM devices (S, T, U and V) in relation to the anatomical

433 structure. (C1) Musculus abductor hallucis. (C2) Musculus flexor hallucis brevis. (C3)

434 Musculus adductor hallucis. The x axis points from the big toe to the heel. The y axis points

435 from digit V to digit I.

436

437 **Figure 2:** Illustration of the methodological considerations. (A) Schematic drawing of a muscle

438 (dark red) and axon of a motor neuron (green) with the motor endplate. Two (v), (-v) action

439 potentials are shown propagating from the endplate to the distal ends of the muscle fibres. The

440 action potential first generates a current with a technical current direction (movement direction

441 of the positive charges) in the direction of the moving action potential. Then, during the

442 repolarisation phase, a current with a technical current in the opposite direction of the

443 propagating action potential is generated. Both currents generate a circular magnetic field in

444 the direction as defined by the right hand rule. (B) Geometrical situation of OPM device (grey),

445 muscle fibre (dark red) and propagating MAP (grey circle with the currents I and movement

446 velocity V). In the figure, d is the shortest distance between the sensor and muscle, l is the

447 longitudinal position of the action potential in relation to the *Lotfußpunkt* (point of shortest

448 distance d to the OPM sensor) and R is the vector connecting the OPM sensor and position of

21

449   action potential with the components. The origin of the coordinate system is defined by the

450   position of the OPM sensor.

451

452   **Figure 3:** Recorded time-dependent magnetic field strength for each OPM sensor (S, T, U and

453   V). (A) Anatomical location of the four OPM sensors (same as Figure 1). (B) Plots of the

454   recorded time-dependent magnetic field strength in the y (left) and z (right) directions for each

455   sensor S, T, U and V (top to bottom). A total of 10 measurements were performed. Each

456   recorded trace is shown as a fine grey line. The first trace – which was used for further analysis

457   – is shown in black. The small horizontal grey lines shown on the plots for the z direction in

458   the time window 5–10 ms correspond to the minimum/maximum of the signal during this

459   period. These maxima were used to approximate the background signal. The red/blue open

460   circles mark the maximum/minimum of the biphasic peaks. The green line on each graph of the

461   y direction marks the second local maximum/minimum. The green line on the graphs of the z

462   direction marks the turning point of the graph. This point corresponds to the time when the

463   action potential passes the *Lotfußpunkt* (point of shortest distance *d* to the OPM sensor).

464

465   **Figure 4:** Comparison of experimentally recorded and modelled magnetic field. For each OPM

466   sensor (S, T, U and V), the recorded magnetic field strength in the y and z direction (red trace)

467   is shown. Based on the finite wire model, the hypothetical sources were modelled, and the

468   corresponding magnetic field strengths were plotted (black traces). The plots on the far right

469   show the presumed offset in the y direction, the longitudinal direction in the xy plane of the

470   muscular fibre (black line) and the direction of the MAP. Note the change in the direction of

471   the MAP between sensors T and U. The MAP likely originated between these two sensors.

472

473

474

475 **Supplementary Figure 1:**

476 Similar Figure as Figure 2 but with the illustration of the magnetic dipole model. Inset in Panel

477 A illustrates how the radial current along the T – tumuli could generate a magnetic dipole.

478 Graphs in Panel C show the signal profile of a simulated moving magnetic dipole.

479

480 **Supplementary Figure 2:**

481 The plot on the left and in the middle show the measured signals for the sensors S, T, U and V

482 top to bottom (red lines). The black line is the result of the simulation based on the magnetic

483 dipole model and model parameters described in the Supplementary Table 1.

484 The axis of abscissae states the distance of the dipole from the "Lotfußpunkt" (point of shortest

485 distance d to the OPM sensor) in cm. The axis of ordinate shows the magnetic field in nano

486 Tesla.

487 The plots on the far right show a two dimensional coordinate system of the xy plane with the z

488 direction point out of the plane and the OPM sensor at the position (x=0,y=0,z=d).

489 The redline on these plots show the linear path of the moving dipole. The blue arrow on the

490 redline points into the direction of movement in relation to time. The red arrow at the centre of

491 origin (x=0, y=0) shows the direction of the magnetic dipole.
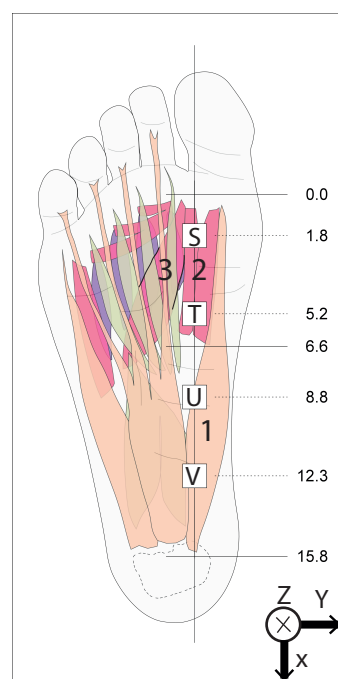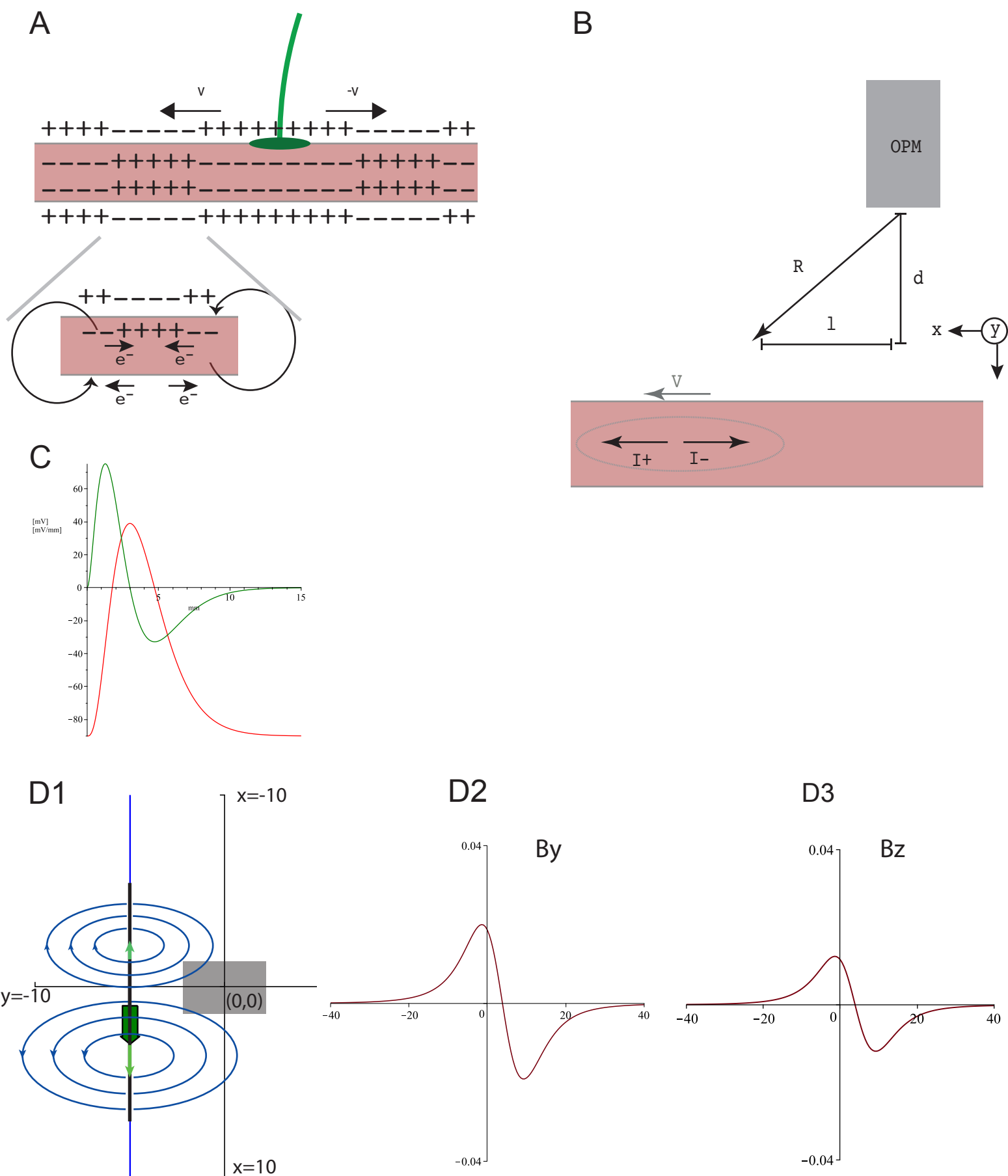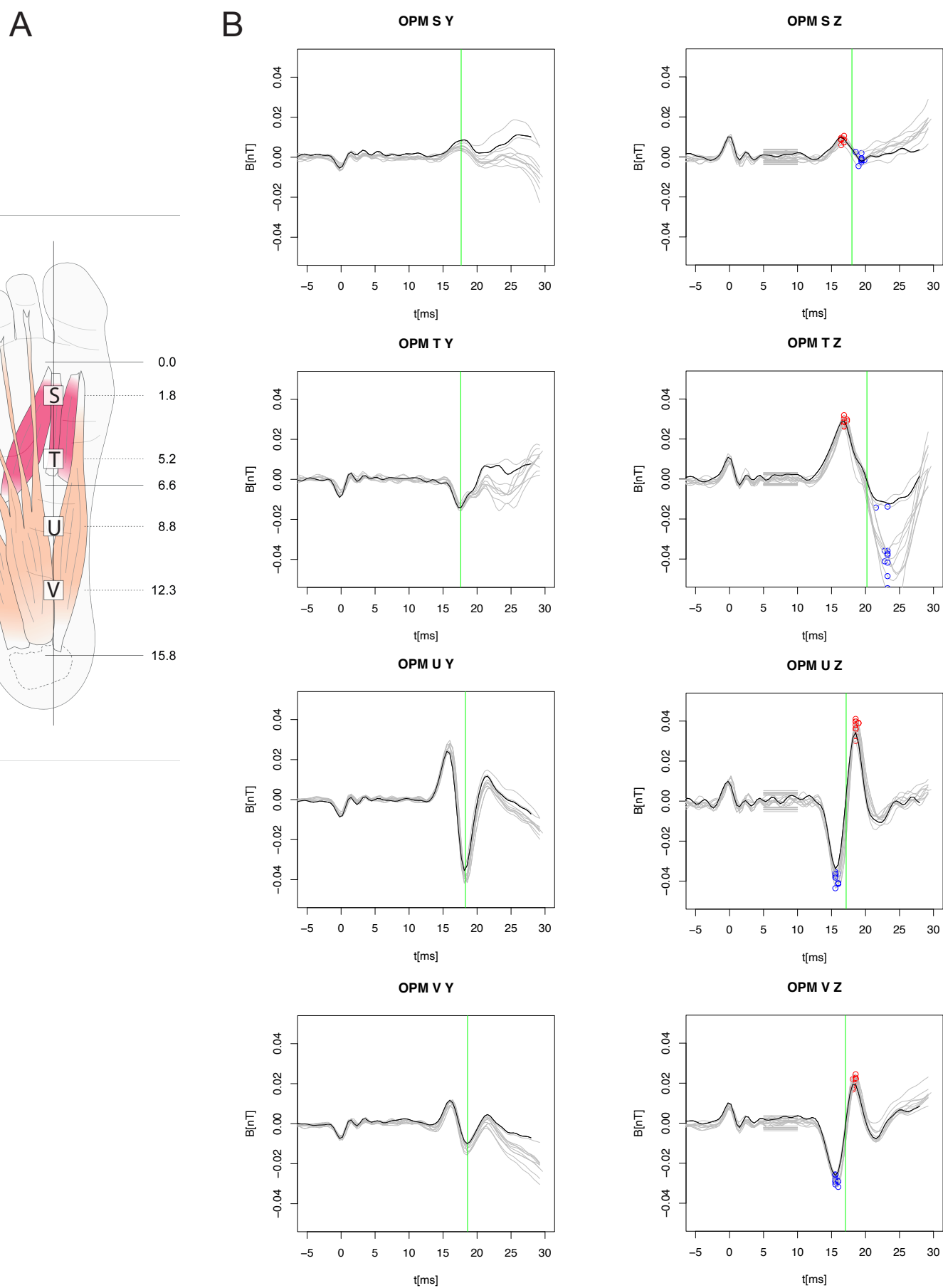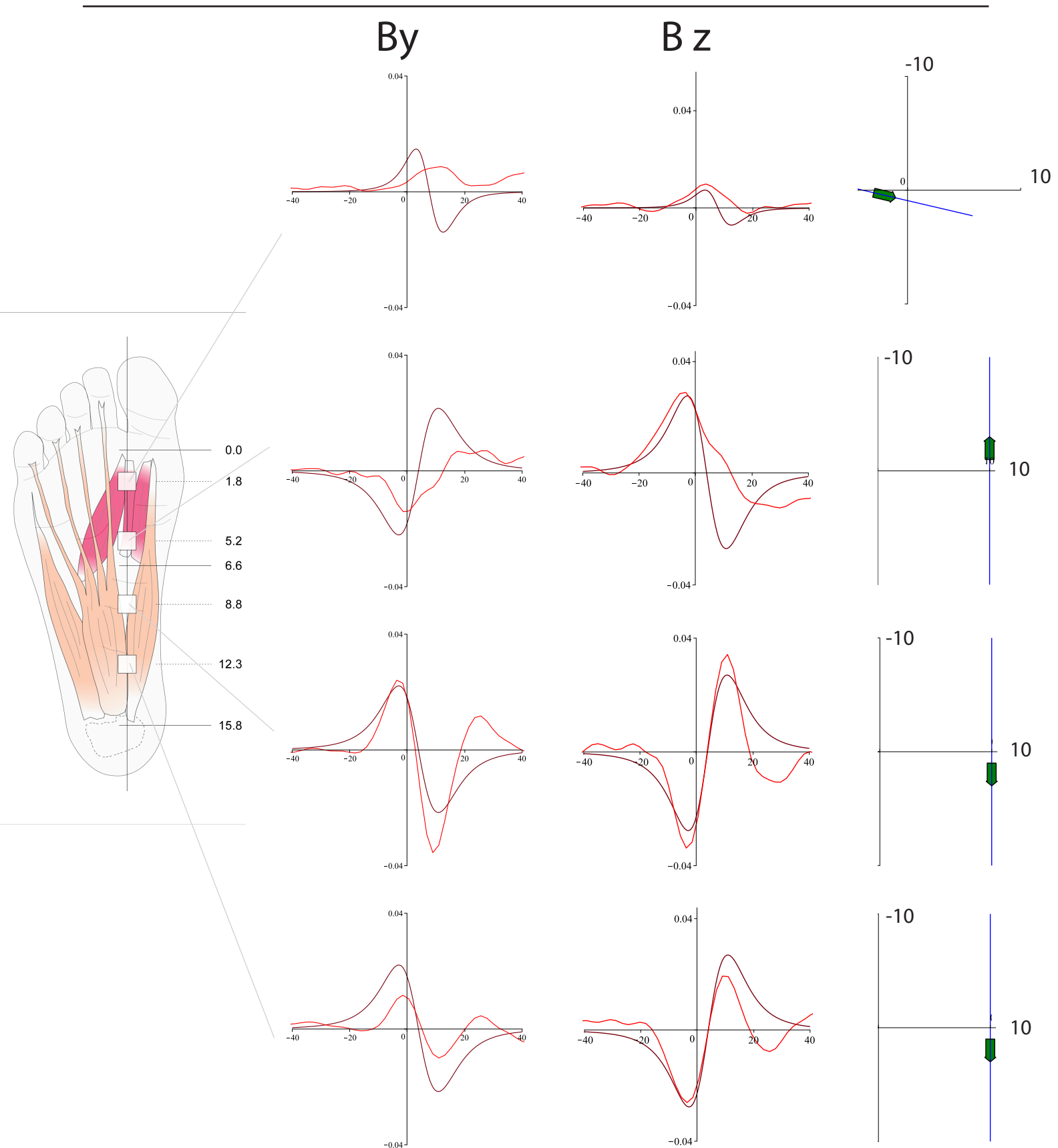
492

Figure 1

A
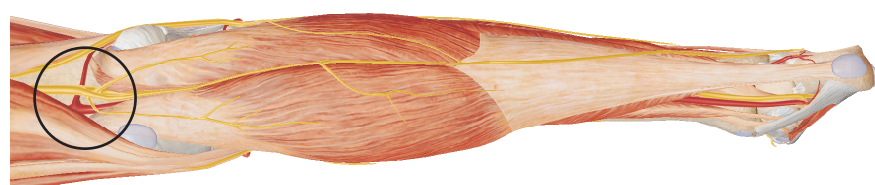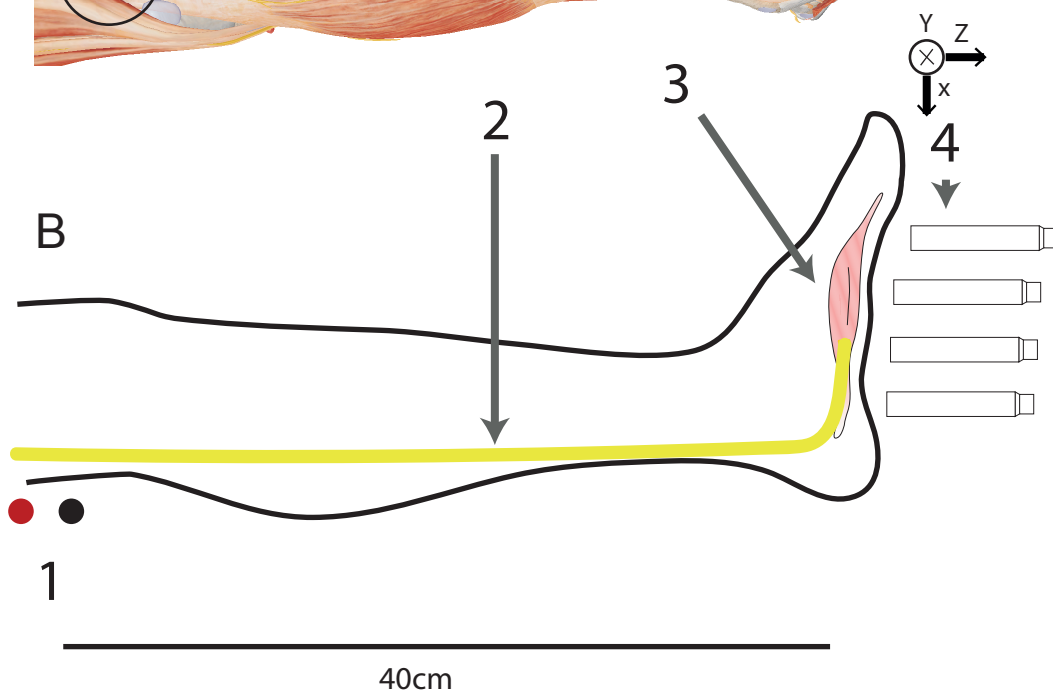
Figure 2

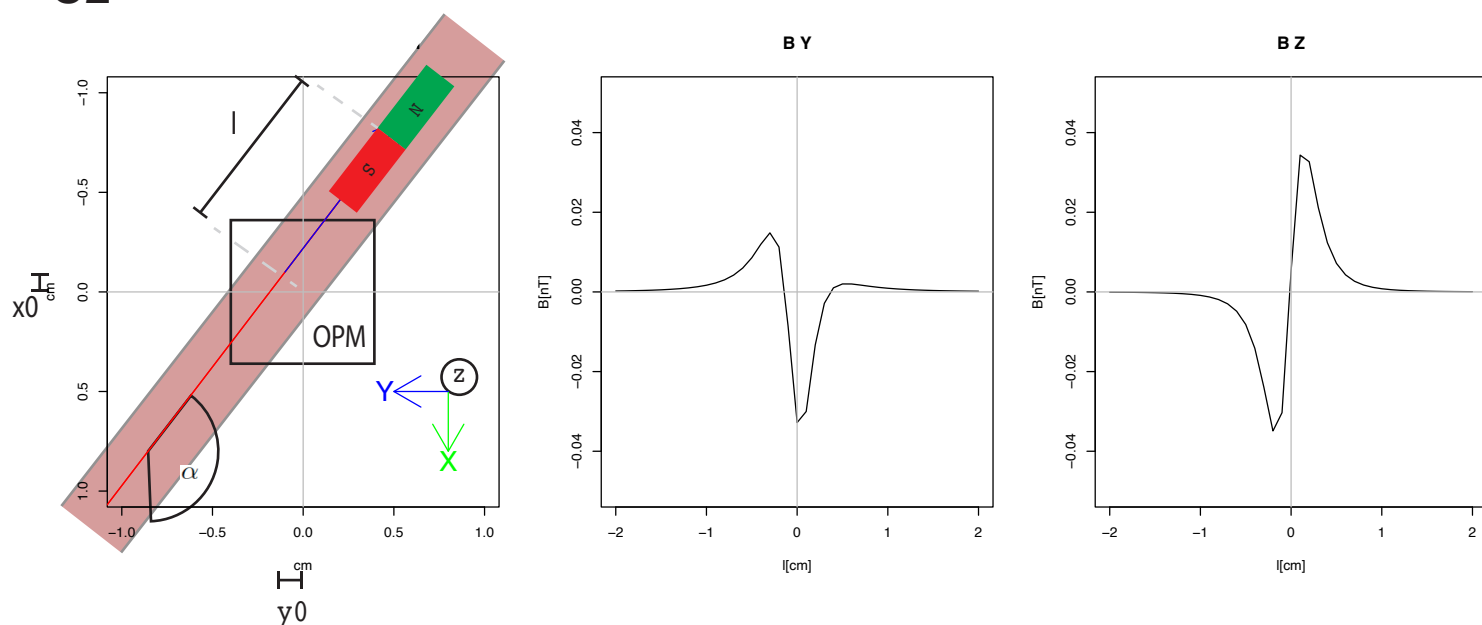# Abbildung 3

Figure 4

Supplementary Fig. 1

A

B

M1

M2

C2

B Y

B Z

Supplementary Fig. 2